

# Chlorella-derived natural photosynthetic system for in situ energy metabolism enhancement in cardiomyocytes

Received: 18 February 2025

Accepted: 22 August 2025

Published online: 30 September 2025

 Check for updates

Yuan Cheng<sup>1,4</sup>, Lijun Lv<sup>1,4</sup>, Zhiqiu Cao<sup>1</sup>, Xiaoqing Huang<sup>1</sup>, Yuqiong Wang<sup>1</sup>, Yue Tang<sup>2</sup>✉, Wen Gao<sup>1</sup>✉ & Bo Tang<sup>1,3</sup>✉

Myocardial ischemia (MI), caused by insufficient blood supply, is a pathological condition where cardiomyocytes lack oxygen and energy supply. Herein, we developed a natural photosynthetic system (HCU) consisting of chlorella pyrenoidosa (*C. pyre*), hyaluronic acid methacryloyl (HAMA) and degradable upconversion nanoparticles (UCNPs, NaCeF<sub>4</sub>:Yb,Tm,Zr). Upon near-infrared irradiation, HCU was photo-crosslinked in situ, thereby facilitating *C. pyre* photosynthetic oxygen generation within the myocardium. Concurrently, cytochrome c oxidase (CCO) in mitochondria was activated to enhance electron transport along the respiratory chain, synergistically boosting cardiac energy metabolism. Consequently, the ATP levels were elevated, and the hypoxic microenvironment was mitigated. In MI mouse models, echocardiography readings returned to normal levels, and the infarct size was significantly reduced following a 7-day treatment with HCU. Based on the photosynthetic system, this study proposes an in situ oxygen and energy metabolic regulation strategy for MI, holding certain inspiration for other ischemia diseases.

Myocardial ischemia (MI) is a pathological condition with an absolute or relative reduction in coronary blood flow (due to coronary artery stenosis, spasm, or embolism), leading to an imbalance between myocardial oxygen supply and energy metabolic demand<sup>1,2</sup>. It mainly manifests as a significant decrease in myocardial oxygen concentrations, triggering mitochondrial energy metabolism dysfunction and insufficient ATP production. Concurrently, the hypoxic microenvironment results in lactate accumulation, reactive oxygen species (ROS) overproduction and calcium ion homeostasis disruption<sup>3</sup>. This cascade induces cardiomyocytes apoptosis and interstitial fibrosis, which ultimately result in cardiac systolic and diastolic dysfunction, clinically manifested as angina pectoris, myocardial infarction, or chronic ischemic heart disease. Clinical treatments for MI, including

drug therapy, interventional therapy and surgical therapy, primarily focus on restoring reperfusion of infarcted blood vessels and improving blood supply to myocardial tissue. While these strategies are essential for alleviating ischemia, they face inherent limitations<sup>4</sup>, such as medication tolerance, restenosis and surgical risk. Moreover, even when revascularization is achieved, these approaches may not fully address mitochondrial energy metabolism dysfunction or sufficiently normalize the hypoxic microenvironment in the injured myocardium<sup>5,6</sup>. In light of these limitations, this study proposes a therapeutic strategy targeting the regulation of mitochondrial energy metabolism and hypoxic microenvironment, which may overcome the bottlenecks of traditional therapies and provide important theoretical basis and translational prospects for MI therapy.

<sup>1</sup>College of Chemistry, Chemical Engineering and Materials Science, Key Laboratory of Molecular and Nano Probes, Ministry of Education, Collaborative Innovation Center of Functionalized Probes for Chemical Imaging in Universities of Shandong, Institutes of Biomedical Sciences, Shandong Normal University, Jinan, China. <sup>2</sup>Department of Emergency Medicine, Shandong Provincial Clinical Research Center for Emergency and Critical Care Medicine, Qilu Hospital of Shandong University, Jinan, China. <sup>3</sup>Laoshan Laboratory, Qingdao, Shandong, China. <sup>4</sup>These authors contributed equally: Yuan Cheng, Lijun Lv.

✉ e-mail: [yuetang0531@hotmail.com](mailto:yuetang0531@hotmail.com); [gaowen@sdnu.edu.cn](mailto:gaowen@sdnu.edu.cn); [tangb@sdnu.edu.cn](mailto:tangb@sdnu.edu.cn)

Photobiomodulation (PBM)<sup>7</sup> is a treatment that uses specific light to promote cell repair and regeneration, which has been applied in biomedical fields, such as wound healing<sup>8,9</sup> and bone tissue regeneration<sup>10</sup>. Previous researchers have demonstrated that light at around 810 nm can enhance the activity of cytochrome c oxidase (CCO)<sup>11–13</sup>. As the fourth central enzyme complex of the mitochondrial respiratory electron transport chain, CCO transfers electrons from cytochrome c to oxygen, creating a proton electrochemical potential energy difference that drives adenosine triphosphate synthase to convert ADP into ATP<sup>14,15</sup>. Consequently, regulating the enzymatic activities in mitochondrial electron respiration chain by PBM can effectively enhance ATP production, thereby addressing energy deficiencies<sup>16</sup>. However, the absence of oxygen in MI condition impairs electron transfer in the mitochondrial respiratory chain<sup>17</sup>. In hypoxic conditions, cardiomyocytes switch to anaerobic respiration, leading to a metabolic crisis that jeopardizes myocardial function and viability<sup>17,18</sup>. Therefore, a single photobioregulatory strategy may not be sufficient to effectively increase ATP levels in MI.

Living microalgae possess superior light-controlled oxygenation capacity through photosynthesis<sup>19</sup>. The intact cell structure of unicellular microalgae protects the inner sophisticated photosynthetic system, ensuring steady oxygen generation in diverse and challenging environments<sup>20,21</sup>. Due to the photosynthetic oxygen production capacity, microalgae have been served as the natural oxygen generator, holding great promise for in vivo applications<sup>22–24</sup>, such as tumor treatment<sup>25</sup> and diabetes wound healing<sup>26</sup>. These biomedical applications demonstrated their biocompatibility in vivo<sup>27,28</sup>. In response to the light at about 475 nm, microalgae can effectively alleviate the hypoxic microenvironment in tissues. However, the limited penetration depth of visible light still poses constraints on its application in deep tissues<sup>29</sup>. In contrast, near-infrared light has a higher penetration depth<sup>30</sup>, while upconversion nanoparticles (UCNPs) can efficiently convert near-infrared light into different UV-visible lights<sup>31,32</sup>. In situ photosynthetic oxygen production may be achieved with the assistance of UCNPs acting as photoconverters. Traditional inorganic UCNPs are susceptible to accumulate in vivo, inevitably leading to acute or chronic toxicity. In recent years, researchers have reported degradable  $K_3ZrF_7:Yb/Er$  and  $Na_3HfF_7:Yb/Er$  with dynamic “soft” lattice<sup>33</sup>. However, the degradation of this material is rapid and uncontrollable, which shortens the residence time of materials at the lesion, resulting in the unsatisfactory treatment results.

In this study, we develop a natural photosynthetic system (HCU) composed of *Chlorella pyrenoidosa* (*C. pyre*),  $NaCeF_4:Yb,Tm,Zr$  (UCNPs) and hyaluronic acid methacrylate (HAMA) for the first time. Based on the UCNP-enabled in situ photobiomodulation and *C. pyre*-derived photosynthetic oxygen generation, we hypothesize that this system (HCU) can synergistically restore oxygen supply and enhance mitochondrial energy metabolism in MI, thereby restoring cardiac function (Fig. 1). Here, by changing the doping amounts of Zr ions, the degradation time of  $NaCeF_4:Yb,Tm,Zr$  can be regulated, which ensures the therapeutic timeliness and reduces the long-term accumulation of UCNPs. Upon excitation at 980 nm, the UCNPs concurrently emit upconversion luminescence at three wavelengths: 365 nm, 475 nm and 800 nm. Specifically, biocompatible natural polymers (HAMA) undergo in situ photocrosslinking (365 nm) and achieve firm adhesion to the myocardium due to dynamic hydrogen bonding. This myocardial patch hydrogel enhances the retention time and stability of UCNPs and *C. pyre* for MI therapy. The *C. pyre* is uniformly distributed in the hydrogel, which can generate oxygen in situ by photosynthesis (475 nm) enhancing the oxygenation saturation in myocardium. The activity of CCO is up-regulated (800 nm), promoting the electron transfer of mitochondrial respiration chain. In summary, HCU leads to a reduction in fibrosis and infarct size, as well as an improvement in cardiac function in MI mouse models by enhancing ATP levels and

mitigating the hypoxic microenvironment. Hence, based on the HCU hydrogel, this study achieves the combination of in situ oxygen production and the photobiomodulation strategy, exhibiting superior cooperative effects in the treatment of MI.

## Results

### Synthesis and characterizations of degradable UCNPs

We synthesized UCNPs ( $NaCeF_4:Yb,Tm,Zr$ ) with controllable biodegradability and good upconversion fluorescence properties using a modified hydrothermal method (Supporting Information). Transmission electron microscopy (TEM), scanning electron microscopy (SEM), and scanning transmission electron microscopy (STEM) images (Fig. 2A, and Supplementary Fig. 1) demonstrated that the synthesized UCNPs exhibited a homogeneous rectangular structure and were well dispersed with a uniform particle diameter of 50 nm. XRD patterns showed all diffraction peaks of synthesized UCNPs matched with  $NaCeF_4$  nanocrystals (JCPDS no. 75-1924), indicating the successful synthesis of  $NaCeF_4$  matrix (Fig. 2D). Notably, XPS (Fig. 2E), EDS (Fig. 2C), corresponding elemental mapping (Fig. 2B) and the right-shift of peaks in XRD implied that doping ions (Yb, Tm and Zr) had been incorporated into the lattice of the  $NaCeF_4$  matrix. Under the 980 nm excitation, the UCNPs emitted light with different wavelengths (Fig. 2F), including 365 nm ( ${}^1D_2 \rightarrow {}^3F_6$ , a four-photon process), 475 nm ( ${}^1G_4 \rightarrow {}^3H_6$ , a three-photon process) and 800 nm ( ${}^1D_2 \rightarrow {}^3F_3$ , a two-photon process) (Fig. 2G and Supplementary Fig. 2). The upconversion luminescence (UCL) properties provide the necessary conditions for UCNPs/*C. pyre*/HAMA (HCU) to achieve in situ crosslinking (365 nm), *C. pyre* photosynthesis (475 nm), and CCO activation (800 nm).

To expand the application of UCNPs in the biomedical field, we also investigated their degradability. The water-soluble  $[ZrF_7]^{4+}$  species possess a propensity to dissolve expeditiously, leading to the  $NaCeF_4$  crystal lattice being destroyed and turning into positive ions and  $[ZrF_7]^{4+}$  clusters (Fig. 2H). To corroborate this mechanism, the synthesized UCNPs were uniformly dispersed in different solutions, including  $KH_2PO_4$  solution (pH 4.8),  $KH_2PO_4-K_2HPO_4$  solution (pH 6.5), Hank's balanced salt solution (pH 7.4), sodium bicarbonate solution (pH 8.3), Tris-HCl (pH 8.8) and sodium hydroxide solution (pH 9.6) (Supplementary Fig. 3). The UCL intensity significantly decreased (Supplementary Fig. 4a, b) after 48 h. Additionally, TEM images showed that the part UCNPs had disintegrated into debris after 48 h in PBS buffer solutions (Fig. 2I). The concentration of degraded Zr manifested a progressive augmentation commensurate with the elapse of time in PBS solutions, while the degradation rate exhibited a corresponding gradual increase with increasing doping of Zr ions (Fig. 2J, K). Nevertheless, in the upconversion emission spectra of UCNPs with varying Zr concentrations, a gradual reduction in luminescence intensity was observed with increasing Zr doping levels (Supplementary Fig. 5). Considering both biosafety and therapeutic efficacy in a comprehensive manner, it is essential to ensure optimal fluorescence intensity alongside material degradation. Therefore, a doping concentration of 10% Zr ions is identified as the most favorable. Thus, we ultimately selected 10% Zr as the final doping content in UCNPs, ensuring an appropriate treatment duration while preventing the long-term accumulation of UCNPs in vivo. Moreover, the bright-blue UCL of UCNPs disappeared after being dispersed in pure water for 48 h (Fig. 2L), further confirming the degradability.

### Synthesis and characterizations of HCU

We prepared a photosynthetic system (HCU) composed of HAMA, *C. pyre* and UCNPs to achieve photosynthesis oxygen generation in the myocardium via in situ photocuring (Fig. 3A). The Fourier transform infrared (FT-IR) spectra indicated the presence of C=O bonding at approximately  $1716\text{ cm}^{-1}$ , suggesting the successful methacrylation of the hyaluronic acid (HA) (Supplementary Fig. 6), which could be photo-crosslinked rapidly in 30 s (Supplementary Fig. 7). The

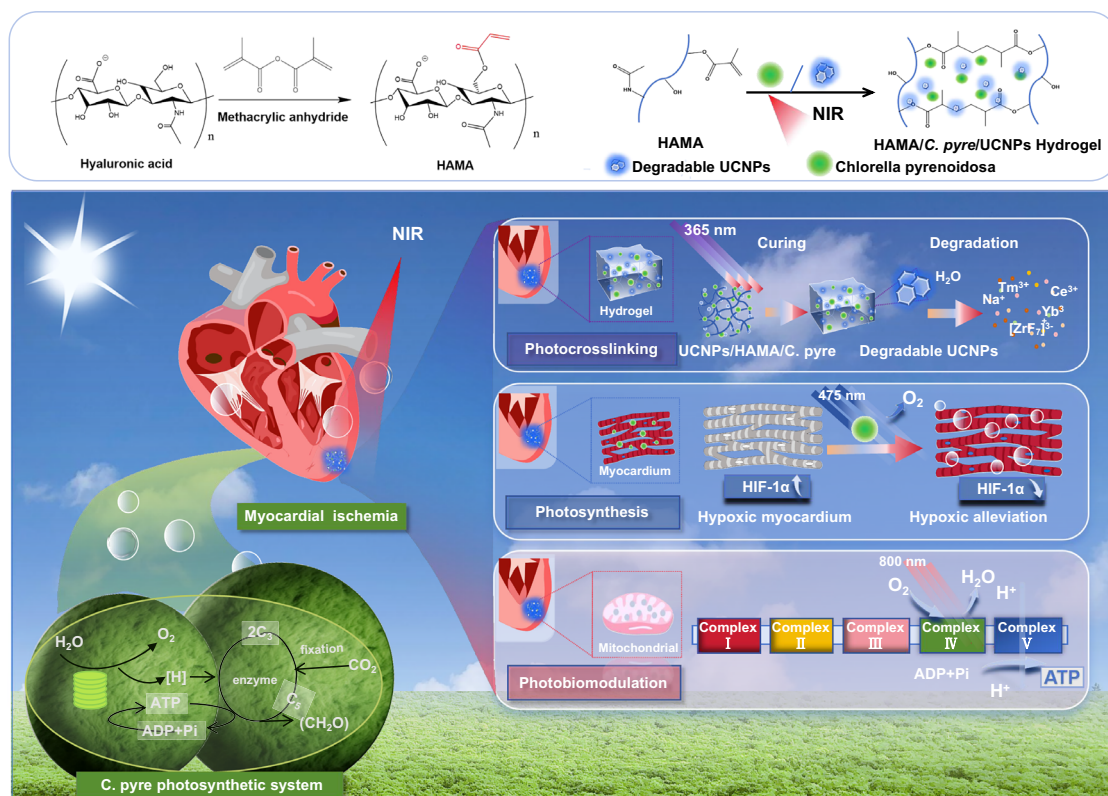


**Fig. 1** | Schematic depictions of natural photosynthetic system for in-situ myocardial ischemic repair.

ultraviolet absorption of LAP coincided with the 365 nm UCL of UCNPs (Fig. 3B). Similarly, the distinct ultraviolet absorption peaks of *C. pyre* were also well-aligned with the 460 nm and 475 nm UCL of UCNPs (Fig. 3B). The spectral overlap provides opportunities for HCU to respond to near-infrared light, facilitating in-situ curing and photosynthesis. Under 980 nm excitation, the simultaneous decrease in UCL intensity of UCNPs at 365 nm, 460 nm, and 475 nm further indicated that LAP and *C. pyre* could be activated by absorbing the UCL of UCNPs (Fig. 3B).

Under 980 nm excitation, HCU was cured in situ through a 10 mm thick chicken muscle tissue (Fig. 3C). The pseudocolor scanning electron microscopy (SEM) image exhibited a tough hydrogel network, while the UCNPs and *C. pyre* were homogeneously distributed in the hydrogel (Fig. 3D). Due to hydrogen bonding between the hydroxyl (-OH) groups of HAMA and the amino (-NH<sub>2</sub>) and sulfhydryl (-SH) groups of tissue, HCU exhibited strong adhesion to tissue surfaces (Fig. 3E, F). Moreover, the cured hydrogel block was completely soluble in PBS after a period of 15 days (Fig. 3G and Supplementary Fig. 8 (a)). Additionally, the fluorescence of UCNPs in the hydrogel gradually disappeared within 14 days (Supplementary Fig. 8 (b)), demonstrating the previous degradation of HCU.

### In situ oxygen-producing capability of HCU

The activity of *C. pyre* was initially confirmed through confocal microscopy imaging by exposing it to blue light (475 nm, 1.0 W/cm<sup>2</sup>). The spherical *C. pyre* emitted bright red fluorescence (Fig. 4A), demonstrating that *C. pyre* exhibited significant biological activity in HCU. Besides, chlorella demonstrated the capacity to survive in HCU for a period exceeding two weeks (Supplementary Fig. 9), thereby substantiating the robust stability of this photosynthetic system. The generation of oxygen from *C. pyre* could be detected by an oxygen indicator probe ([Ru(dpp)<sub>3</sub>]Cl<sub>2</sub>, RDPP). As a result, the variation of fluorescence intensity indicated that soluble oxygen concentration of the *C. pyre* solution increased under adequate light conditions

(475 nm, 1.0 W/cm<sup>2</sup>) and decreased in the dark (Fig. 4B), which demonstrated that the *C. pyre* was fully active to carry out photosynthesis. Under 475 nm excitation with a power density of 1.0 W/cm<sup>2</sup>, the oxygen production rate was positively correlated with the *C. pyre* concentration, which was the optimal at the 1 × 10<sup>8</sup>/mL *C. pyre* group (Supplementary Fig. 10 (a)).

In addition, *C. pyre*, HAMA/*C. pyre* (HC) and HAMA/*C. pyre*/UCNPs (HCU) were subjected to 980 nm laser irradiation with a power density of 1.0 W/cm<sup>2</sup>. The variation of RDPP fluorescence intensity in the system was measured every 2 min for a total duration of 30 min. As expected, the fluorescence intensity gradually decreased, validating that *C. pyre* in the HCU (NIR) group could generate oxygen effectively (Fig. 4C). Likewise, HCU was exposed to 980 nm laser irradiation with different intensities (Supplementary Fig. 10b), indicating that the oxygen production efficiency of *C. pyre* increased with increasing laser power. Considering the biosafety and temperature, we chose 1.0 W/cm<sup>2</sup> as the final power.

### Reversion of hypoxic microenvironment via HCU

Biocompatibility is critical for the clinical applications of biomaterials, thus the biocompatibility of HCU was evaluated by CCK-8 method. During the incubation with HCU, the cell viability of cardiomyocytes (H9c2) all remained more than 85%, indicating HCU had no apparent cytotoxicity (Supplementary Fig. 11).

Myocardial ischemia is typically accompanied by a hypoxic microenvironment. We induced hypoxia in cardiomyocytes using the oxygen and glucose deprivation (OGD) method (Fig. 4D). To investigate the impact of HCU on cardiomyocytes, we assessed the changes in oxygen concentration using an RDPP probe. Under 980 nm irradiation, H9c2 cells treated with HCU (NIR) exhibited a significant decrease in RDPP fluorescence intensity, indicating the photosynthetic oxygen generation capability of HCU (Fig. 4E, G, and Supplementary Fig. 12).

Furthermore, the capacity of the photosynthetic system to alleviate hypoxia was evaluated in vitro through immunofluorescence

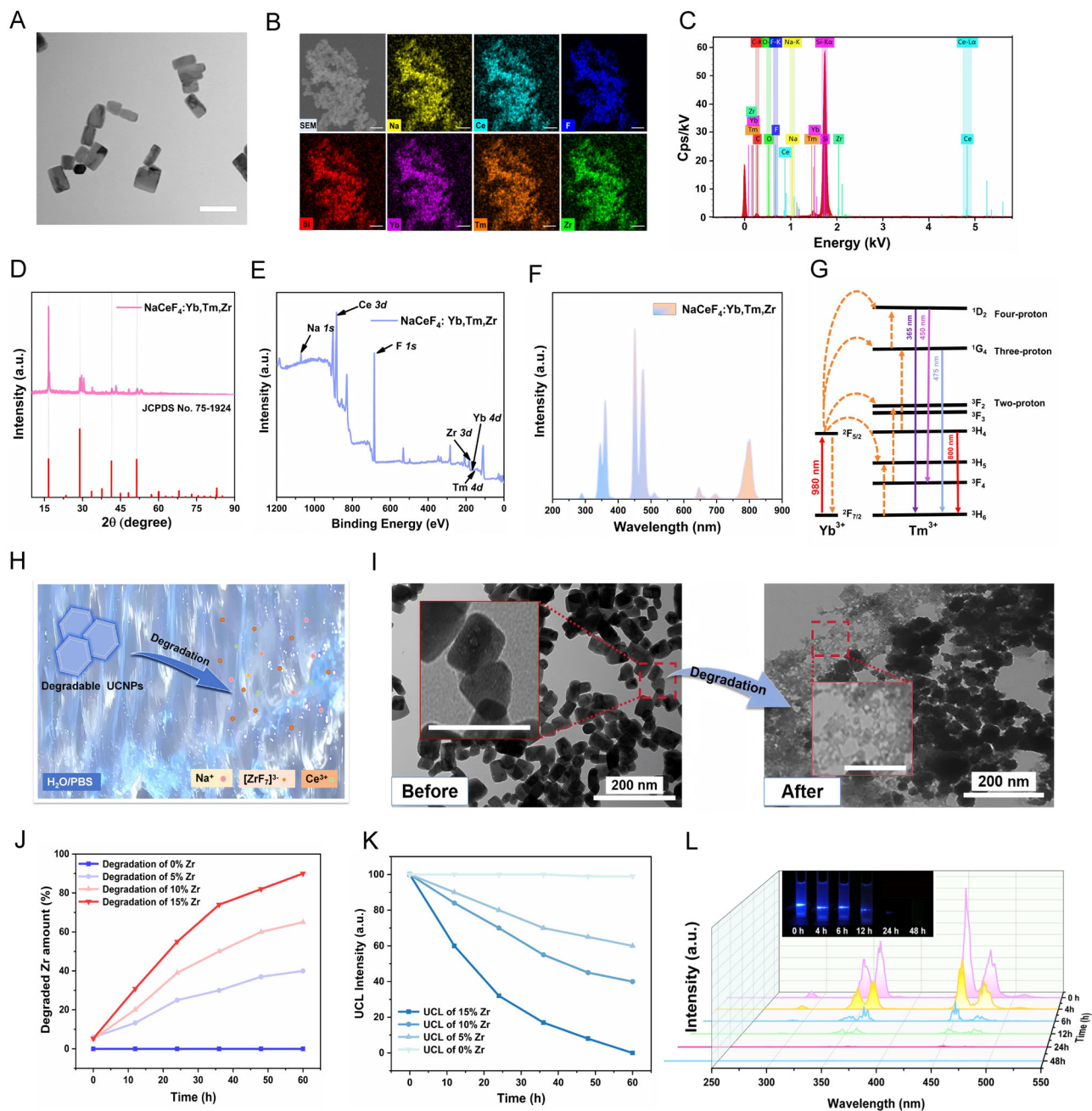


**Fig. 2 | Characterizations of degradable NaCeF<sub>4</sub>:Yb,Tm,Zr UCNPs.** **A** TEM image (scale bar: 50 nm), **B** corresponding elemental mapping images of NaCeF<sub>4</sub>:Yb,Tm,Zr, **C** EDS analysis, **D** XRD patterns and **E** XPS spectrum. **F** Upconversion emission spectrum of NaCeF<sub>4</sub>:Yb,Tm,Zr upon excitation at 980 nm with a power density of 1.0 W/cm<sup>2</sup>. **G** Proposed energy transfer mechanism. **H** Schematic diagram of the degradation process of UCNPs. **I** TEM images before (left) and after (right) dispersing NaCeF<sub>4</sub>:Yb,Tm,Zr in PBS buffer solutions for 48 h.

(Partial enlarged images, scale bar: 100 nm.) **J** Accumulated release profiles of degraded Zr component and **K** UCL intensity for the 475 nm emission over time when dispersing NaCeF<sub>4</sub>:Yb,Tm,Zr into PBS buffer solutions. **L** Upconversion emission spectrum and photographs of UCL brightness over time at deionized water upon 980 nm laser excitation with a power density of 1.0 W/cm<sup>2</sup>. Independent experiments were performed ( $n = 3$ ) for (**A**, **I**) with similar results. Source data are provided as a Source Data file.

staining for hypoxia-inducible factor-1 $\alpha$  (HIF-1 $\alpha$ ), which serves as an oxygen receptor in cells. Consequently, H9c2 cells in the MI group displayed pronounced red fluorescence of HIF-1 $\alpha$  when compared to those under normoxic conditions (Fig. 4F). In marked contrast, the intensity of red fluorescence exhibited a significant decrease in HCU (NIR) group, indicating the prior hypoxia alleviation effect of HCU (Fig. 4F, H, and Supplementary Fig. 13). We further validated this conclusion in primary cardiomyocytes (PCMs) of neonatal mice. The results demonstrated that HCU could effectively reverse the hypoxic microenvironment of PCMs when exposed to 980 nm laser

(1.0 W/cm<sup>2</sup>), which is consistent with the aforementioned findings in H9c2 cells (Supplementary Fig. 14).

In addition, we also assessed the biocompatibility and oxygen-producing activity of *C. pyre* cocultured with human-derived cells (Human Umbilical Vein Endothelial Cells, HUVECs). HUVECs were cultured with HCU (*C. pyre*,  $1 \times 10^8$  cells/ml) under normoxic conditions. Under irradiation at 475 nm, live/dead cell staining assay demonstrated good activity of HUVECs (green) and *C. pyre* (red), indicating that *C. pyre* exhibits fine biocompatibility with human cells (Supplementary Fig. 15). Furthermore, the changes in oxygen

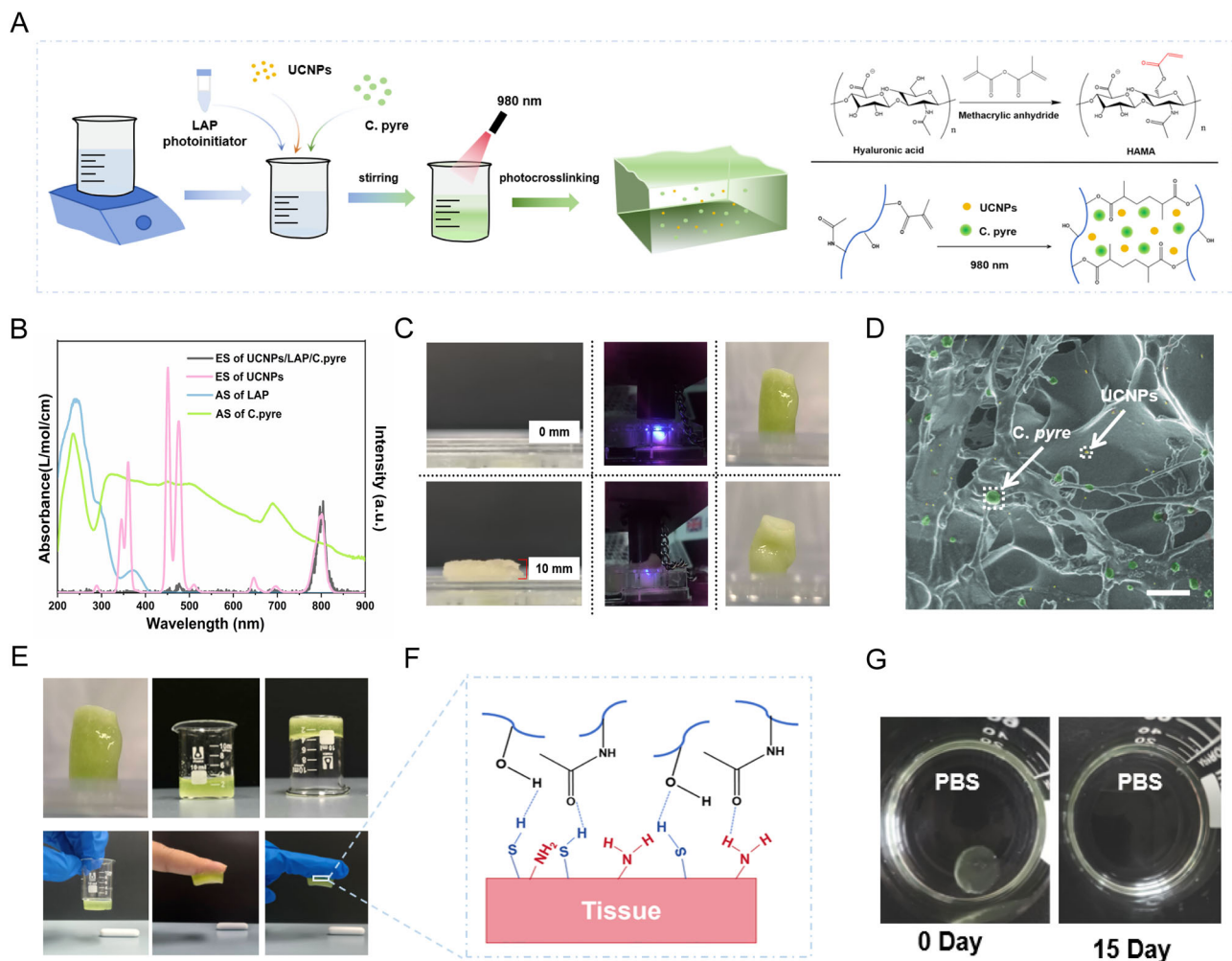


**Fig. 3 | Preparation and characterization of HAMA/*C. pyre*/UCNPs (HCU).**

**A** The preparation process of in-situ photosynthetic system and photocrosslinking mechanism. **B** Absorption spectra of LAP (blue), *C. pyre* (green) and upconversion emission spectra of  $\text{NaCeF}_4:\text{Yb,Tm,Zr}$  (pink) upon excitation at 980 nm with a power density of  $1.0 \text{ W/cm}^2$ . **C** Photographs of NIR photocuring HCU covered over

by chicken tissue with 10 mm thickness. **D** Pseudocolor SEM image of *C. pyre* (green) and UCNPs (yellow) within the HCU. Scale bar, 10  $\mu\text{m}$ . **E** Adhesion of HCU with surfaces of various substrates. **F** Adhesion mechanism of the HCU gel. **G** The degradation process of HCU in the PBS. Independent experiments were performed ( $n = 3$ ) for **(D)** with similar results. Source data are provided as a Source Data file.

concentration were assessed via the RDPF probe. The *C. pyre* group exhibited a progressively lower fluorescence intensity than the *C. pyre* + HUVECs group (Supplementary Fig. 16, 17), demonstrating that the oxygen produced by *C. pyre* was utilized by HUVECs.

Moreover, we examined the apoptosis of cardiomyocytes induced by hypoxic conditions. Hypoxia activates various apoptotic pathways within cells. As expected, the HCU (NIR) treatment down-regulated the protein expression level of HIF-1 $\alpha$  induced by hypoxia, indicating the alleviation of hypoxic microenvironment (Fig. 4I). Simultaneously, the anti-apoptotic protein expression of Bcl-2 was up-regulated and inhibited the release of cytochrome c from the mitochondria. The expression of the anti-apoptotic protein C-Caspase3 was down-regulated, further indicating that the activation of the caspase pathway was suppressed in the HCU (NIR) group (Fig. 4I–M). Furthermore, flow cytometry was used to further evaluate the treatment effects of cardiomyocyte apoptosis induced by hypoxia (Fig. 4N). The apoptosis rate of cardiomyocytes in hypoxia group was 23.91%, and the apoptosis rate of the HCU (NIR) group significantly decreased to 8.72% (Fig. 4N, O and Supplementary Fig. 18). These results suggested that HCU significantly inhibited the apoptosis of cardiomyocytes induced by hypoxia.

### Restoration of energy metabolism via HCU

Mitochondria play a critical role in supplying energy to myocardial tissues. Endowing hydrogels with mitochondrial protective properties represents an effective strategy to prevent the progression of myocardial ischemia. The mitochondrial morphology of cardiomyocytes was assessed using transmission electron microscopy (TEM) (Fig. 5A). Compared with the normal group, mitochondria under hypoxic conditions exhibited a rounded morphology, and the matrix density decreased. Additionally, the cristae were markedly reduced, shortened, or even completely absent, indicative of significant mitochondrial damage. In marked contrast, the mitochondria in the HCU (NIR) group ( $980 \text{ nm}$ ,  $1.0 \text{ W/cm}^2$ ) exhibited a rod-like morphology characterized by smooth outer membranes and inner membranes folded into cristae of varying lengths, closely resembling those of normal mitochondria (Fig. 5B, C). The restoration of mitochondrial morphology suggested that HCU could mitigate mitochondrial injury induced by hypoxia.

Photobiomodulation (PBM) is a therapeutic approach, which could enhance adenosine triphosphate (ATP) synthesis by up-regulating the activity of cytochrome c oxidase (CCO). During the oxidative phosphorylation process, the proton pump establishes a transmembrane potential by transporting protons. The damage of the

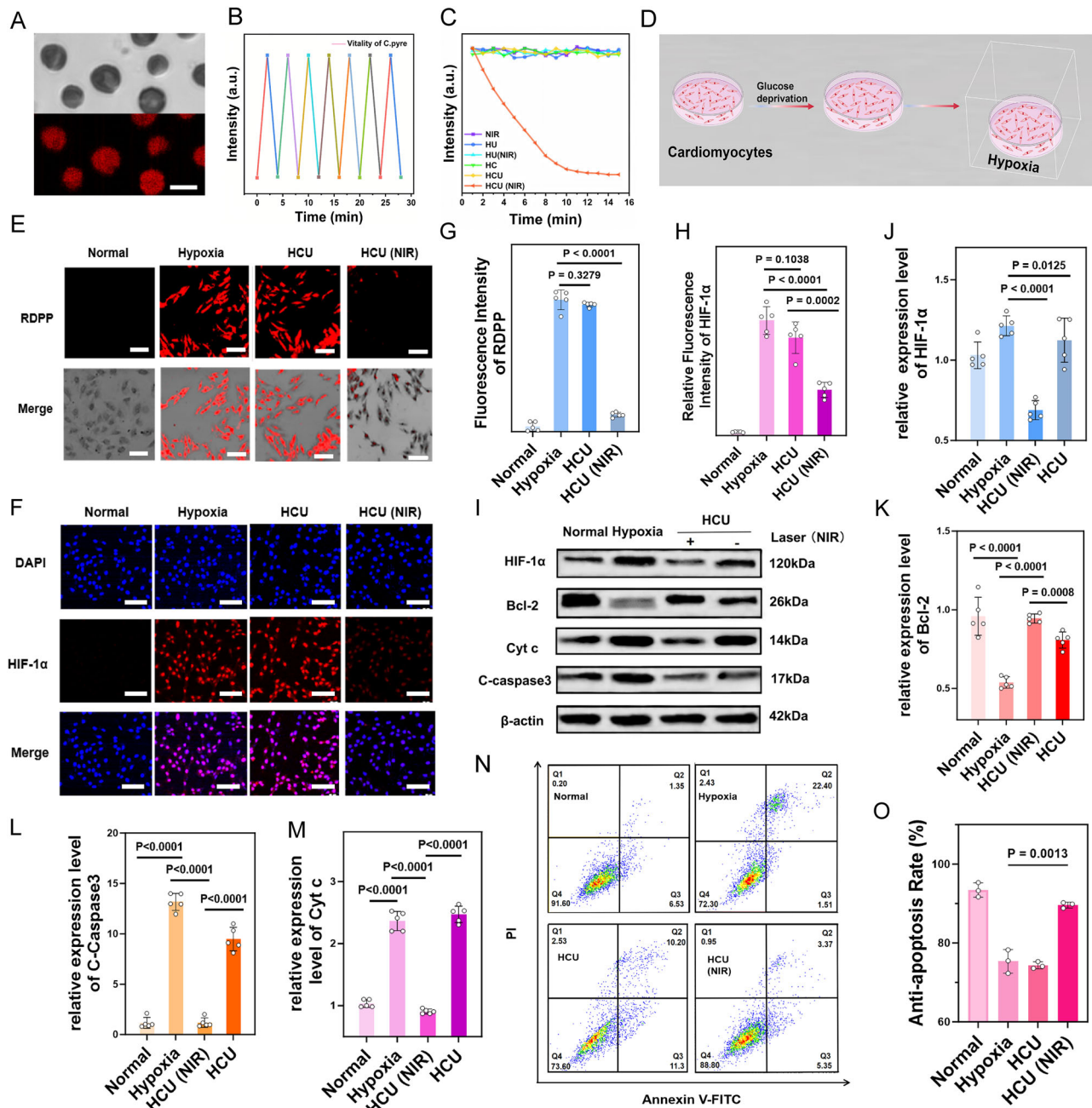


**Fig. 4 | Validation of the alleviating hypoxia capacity and anti-apoptotic effects of photosynthetic system on cardiomyocytes.** **A** Bright-field and fluorescence-field images of *C. pyre* in HAMA, scale bar, 5  $\mu\text{m}$ . **B** Activity of *C. pyre*. **C** Dissolved  $\text{O}_2$  level changes of the solution containing HCU with various treatments. **D** Flow chart of induced hypoxia in cardiomyocytes. **E** Fluorescence images of H9c2 cells staining with RDPP probe after various treatments. **F** Fluorescence images of H9c2 cells staining with HIF-1 $\alpha$  antibody (red) and DAPI (blue) after various treatments, scale bar: 50  $\mu\text{m}$ . **G** Quantitative fluorescence analysis of RDPP probes ( $n = 5$ ,  $n$  represent the number of independent experiments, mean  $\pm$  s.d.). **H** Quantitative fluorescence analysis of HIF-1 $\alpha$  ( $n = 5$ ,  $n$  represent the number of independent experiments, mean  $\pm$  s.d.). **I** The levels of proteins including HIF-1 $\alpha$ , Bcl-2, C-Caspase 3 and Cyt c in H9c2 cells analyzed by western blotting. **J–M** Corresponding quantitative histograms of protein expression ( $n = 5$ ,  $n$  represent the number of independent experiments, mean  $\pm$  s.d.). **N** Anti-apoptosis analysis of H9c2 cells by flow cytometry after various treatments. **O** Corresponding quantitative histograms of anti-apoptosis rate ( $n = 3$ ,  $n$  represent the number of independent experiments, mean  $\pm$  s.d.). Statistical analysis was performed using unpaired two-tailed Student's *t* test. Independent experiments were performed ( $n = 3$ ) for (A) with similar results. Source data are provided as a Source Data file.

experiments, mean  $\pm$  s.d.). **I** The levels of proteins including HIF-1 $\alpha$ , Bcl-2, C-Caspase 3 and Cyt c in H9c2 cells analyzed by western blotting. **J–M** Corresponding quantitative histograms of protein expression ( $n = 5$ ,  $n$  represent the number of independent experiments, mean  $\pm$  s.d.). **N** Anti-apoptosis analysis of H9c2 cells by flow cytometry after various treatments. **O** Corresponding quantitative histograms of anti-apoptosis rate ( $n = 3$ ,  $n$  represent the number of independent experiments, mean  $\pm$  s.d.). Statistical analysis was performed using unpaired two-tailed Student's *t* test. Independent experiments were performed ( $n = 3$ ) for (A) with similar results. Source data are provided as a Source Data file.

mitochondrial respiratory chain leads to a reduction in mitochondrial membrane potential. Consequently, measurement of mitochondrial membrane potential was employed to evaluate the degree of respiratory chain damage and the energy metabolism. The green fluorescence of the JC-1 fluorescent probe within the mitochondrial matrix were triggered in the presence of a low mitochondrial membrane potential. As expected, both the HCU (NIR) and HU (NIR) prevented the decrease

of the mitochondrial membrane potential (MMP) in a hypoxia environment. Compared with the HU (NIR) group, the HCU (NIR) group showed a more significant inhibitory effect on MMP decline (Fig. 5D, H and Supplementary Fig. 19), demonstrating that the combination of oxygen generation and photobiomodulation provided better protective effect on mitochondria. We further evaluated the above effect of HCU using PCMs. With the irradiation of NIR laser (980 nm, 1.0 W/cm<sup>2</sup>),

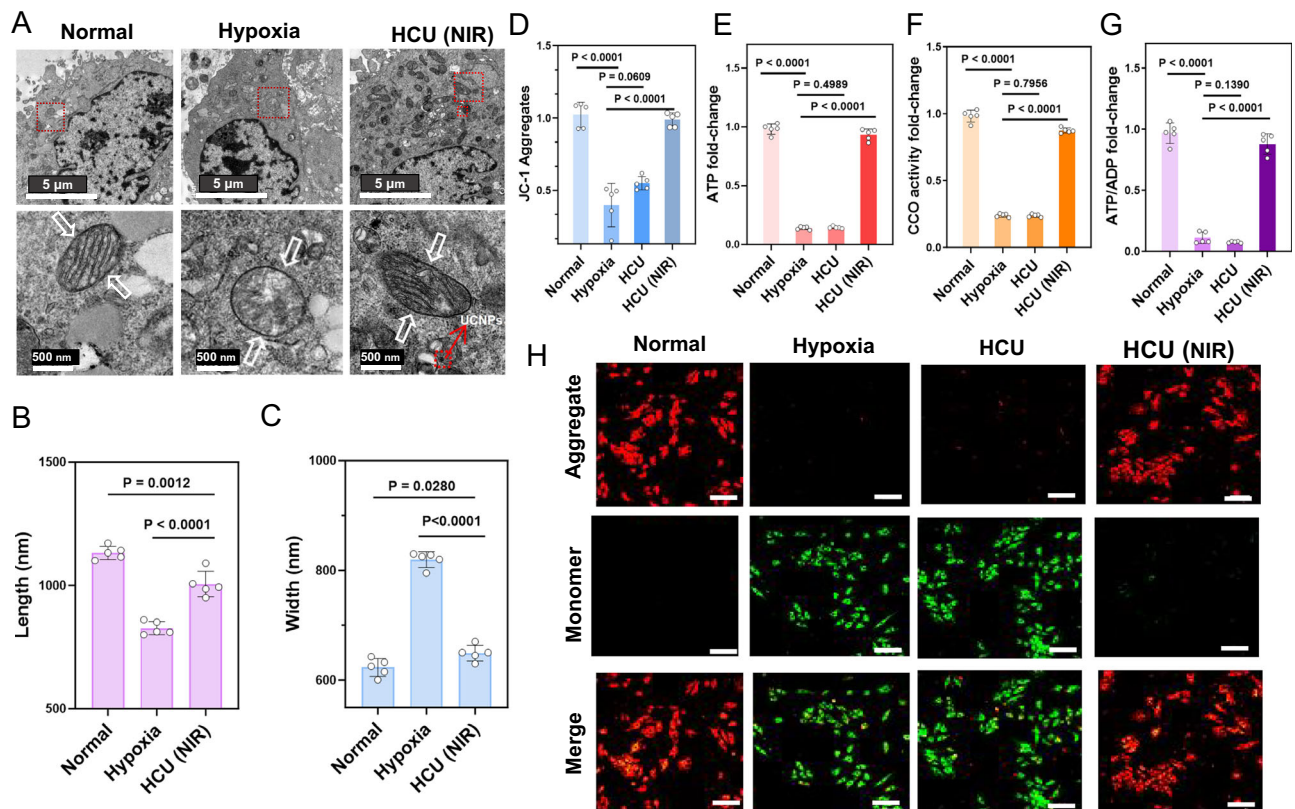


**Fig. 5 | Mitochondrial function repair capacity of the hydrogel.** **A** BiO-TEM images of H9c2 cells showing the morphological changes of mitochondria, scale bar: 500 nm. **B, C** The lengths, widths of mitochondria ( $n = 5$ ,  $n$  represent the number of independent experiments, mean  $\pm$  s.d.). **D** Fluorescence quantification of JC-1 aggregates ( $n = 5$ ,  $n$  represent the number of independent experiments, mean  $\pm$  s.d.). **E** ATP fold-change after different treatment ( $n = 5$ ,  $n$  represent the number of independent experiments, mean  $\pm$  s.d.). **F** CCO activity fold-change after different treatment ( $n = 5$ ,  $n$  represent the number of independent experiments,

mean  $\pm$  s.d.). **G** ATP/ADP fold-change after different treatment ( $n = 5$ ,  $n$  represent the number of independent experiments, mean  $\pm$  s.d.). **H** Fluorescence images of H9c2 cells staining with JC-1 kit in Normal group, Hypoxia group, NIR group (980 nm, 1.0 W, 20 min), HC (HAMA/C. *pyre*) group, HC (NIR) group, HU (HAMA/UCNPs) group, HU (NIR) group, HCU (HAMA/C. *pyre*/UCNPs) group, HCU (NIR) group. Scale bar, 20  $\mu$ m. Statistical analysis was performed using unpaired two-tailed Student's *t* test. Source data are provided as a Source Data file.

HCU also suppressed the decline of MMP in hypoxic PCMs (Supplementary Fig. 20), concurring with the aforementioned findings in H9c2 cells.

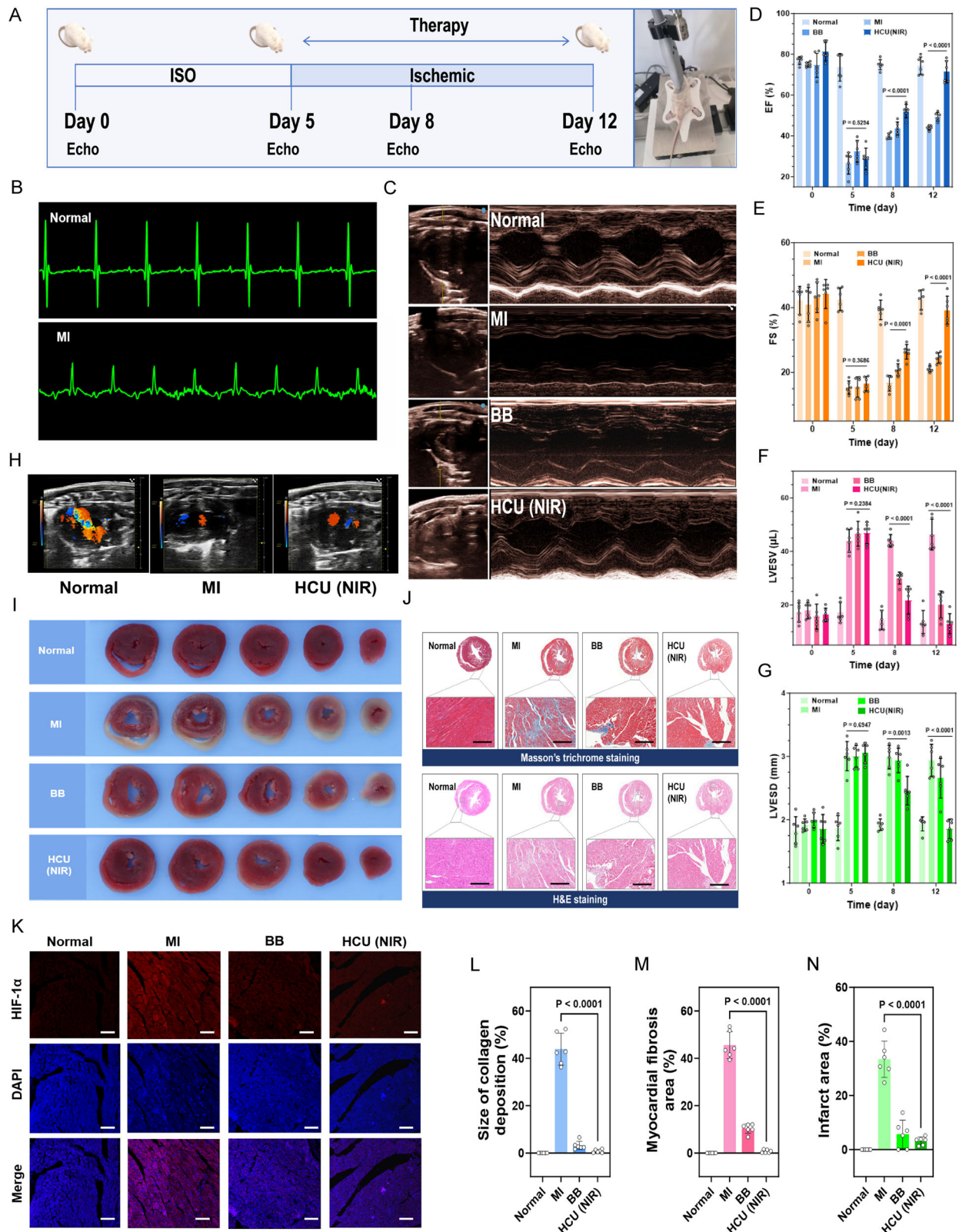
Sufficient ATP supply is the basis for ensuring myocardium activity. Protecting energy metabolism is an effective way to recover cardiac function. To validate the photobiomodulation effect, we measured the activity of CCO. As a result, the CCO activity was found to increase in the HU (NIR) group and the HCU (NIR) group, indicating that the UCL of UCNPs improved the activity of CCO by PBM (Fig. 5F, Supplementary Fig. 21a). Light-controllable effect of HCU on cell metabolism was then assessed. After 10 min of radiation by 980 nm laser (1.0 W/cm<sup>2</sup>), the ATP level increased in both HU (NIR) group and HCU (NIR) group, while the ATP level in HCU (NIR) group was close to that noted in the normal group (Fig. 5E and Supplementary Fig. 21b). These results indicated that in situ oxygen supply further stimulated the generation of ATP. We then adjusted the light intensity and irradiation time to optimize the experimental conditions. As the laser frequency increased over a period of 10 min, a peak was observed at an output power of 1.0 W (Supplementary Fig. 22a). The ATP levels rose until they reached a state of stabilization within 20 min of light exposure (Supplementary Fig. 22b). Moreover, the level of ATP/ADP also increased in the HCU (NIR) group (Fig. 5G and Supplementary Fig. 23), further showing that the recovery of the respiration chain stimulated the conversion of ADP to ATP. These results further indicated that the photosynthetic system could achieve the cooperative interaction of oxygen generation and photobiomodulation to improve energy metabolism in cardiomyocytes.

### In vivo myocardial ischemia therapeutic effects of HCU

To evaluate the therapeutic effect of HCU on myocardial infarction (MI), we induced MI in mouse models using isoproterenol (ISO, a non-selective  $\beta$ -adrenergic receptor agonist) (Fig. 6A). Following ISO induction, the electrocardiogram (ECG) of mice exhibited markedly elevated ST segments, deepened pathological Q-waves, inverted T-waves, and prolonged QRS durations (Fig. 6B). Concurrently, echocardiography revealed a significant decrease in ejection fraction (EF) and fractional shortening (FS), indicating successful induction of the MI model (Fig. 6C). These MI mice were then randomly divided into three groups: MI group, BB group (treated with Metoprolol Tartrate;  $\beta$ 1-adrenergic receptor antagonists), and HCU (NIR) group.

Due to the lack of oxygen supply, cardiac function tended to decline over 7 days in the MI group (Fig. 6C, D). In contrast, the HCU (NIR) recovered the EF, FS, left ventricular end-systolic dimension (LVESD) and left ventricular end-systolic volume (LVESV) (Fig. 6C–G) of MI mice after treatment, which were approaching the healthy value and more effective than the BB group. Moreover, we evaluated the long-term effects via echocardiography. Mice in HCU (NIR) group continued to maintain the normal EF, FS, LVESV and LVESD at 30 days (Supplementary Fig. 27), which were similar with the healthy value, preliminarily suggesting that HCU (NIR) had long-term effects on the myocardial activity recovery. Color Doppler Flow Images (Fig. 6H) further indicated that HCU (NIR) recovered the myocardial activity and inhibited myocardial injury by oxygen supply and photobiomodulation.

TTC staining was utilized to further assess the extent of the infarct in the MI model (Fig. 6I and Supplementary Fig. 24). The infarct area

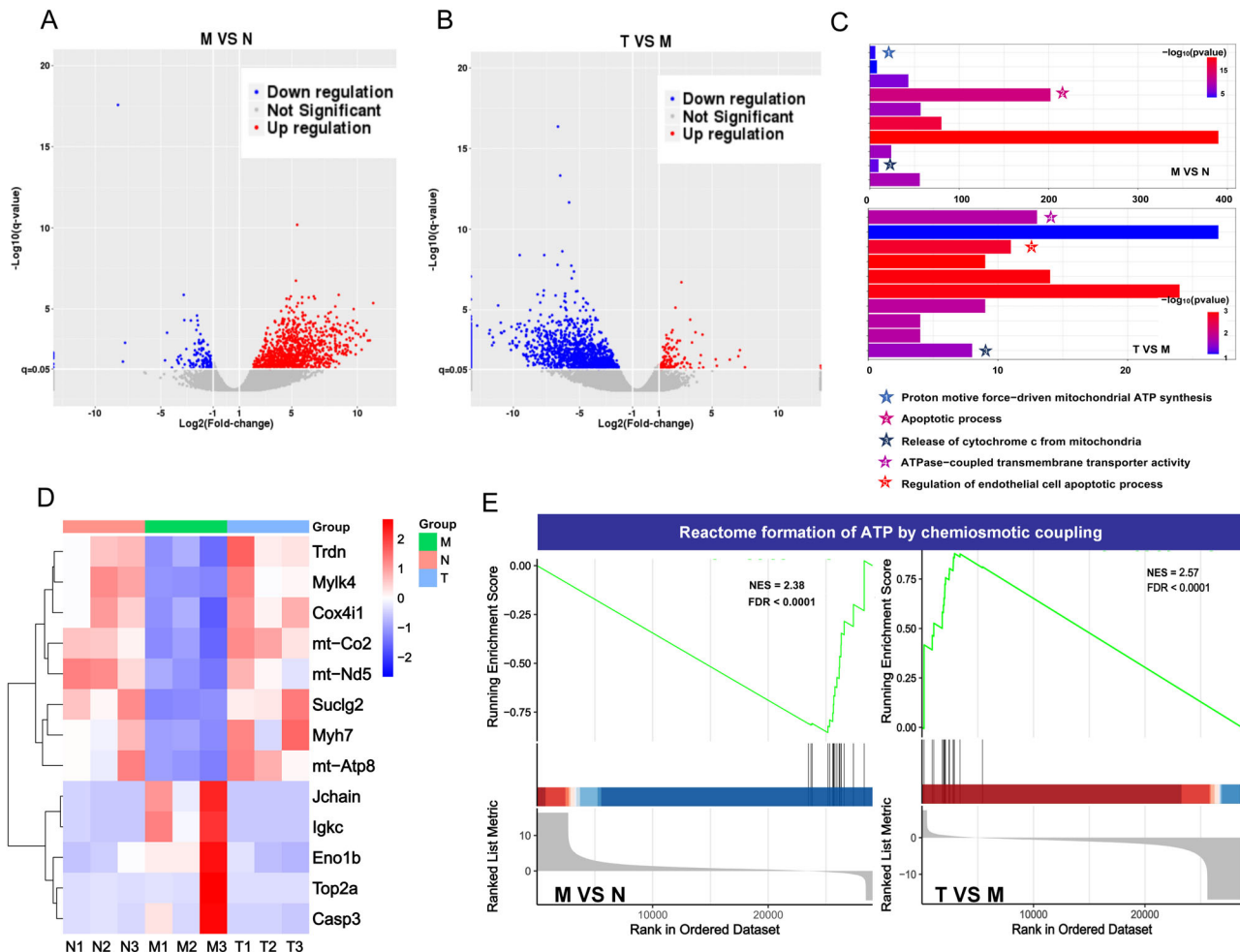


was significantly reduced from  $33.38\% \pm 6.69\%$  to  $3.20\% \pm 1.47\%$  in the HCU (NIR) group, which was comparable to that in the Normal group and superior to the BB group (Fig. 6I and N). This result suggested that HCU could reverse myocardial injury induced by ISO. Hematoxylin-eosin staining and Masson's trichrome staining were used to assess the therapeutic effect of different treatments on myocardial repair (Fig. 6J). The MI group exhibited malignant ventricular remodeling,

such as myocardial fibrosis and collagen deposition. Conversely, the BB group and HCU (NIR) group had more myocardial fibers (red) survival and fewer collagen deposition (blue), especially in the HCU (NIR) group (Supplementary Fig. 25, 26). Moreover, HCU prevented further infarct expansion and fibrotic deposition, thus reducing the infarct area (Fig. 6J) and L-N). These results indicated that ventricular remodeling could be suppressed by oxygen generation and

**Fig. 6 | In vivo therapeutic efficacy of photosynthetic system in myocardial ischemia mice.** **A** Schematic illustration of the animal treatment protocol in the MI model. **B** ECG of mice before (left) and after (right) induction. **C** Echocardiography of mice in different treatment groups after treatment for 7 days. **D–G** Quantitative analysis of the EF, FS, LVESV and LVESD at different periods ( $n = 6$ ,  $n$  represent biologically independent animal samples in each group, mean  $\pm$  s.d.). **H** Representative images of the mouse ischemic cardiac detected by Color Doppler Flow Imaging. **I** TTC staining of hearts from mice in different groups. **J** Masson

trichrome staining displayed the fibrous tissue (blue) and myocardium (red) and HE trichrome staining of sections of hearts from mice in different groups, scale bar: 100  $\mu$ m. **K** HIF-1 $\alpha$  (red) and DAPI immunostaining (blue) of myocardium in different groups, scale bar: 50  $\mu$ m. **L–N** Quantitative analysis of collagen area, fibrosis area, infarct area ( $n = 6$ ,  $n$  represent biologically independent animal samples in each group, mean  $\pm$  s.d.). Statistical analysis was performed using unpaired two-tailed Student's  $t$  test. Source data are provided as a Source Data file.



(MI vs Normal and HCU vs MI).  $n = 3$ ,  $n$  represent biologically independent animal samples in each group. The  $P$  values were determined using the negative binomial distribution, and then the Benja mini-Hochberg procedure was used for multiple hypothesis testing correction.

photobiomodulation. In a word, analysis of cardiac function and histopathological assessment suggested that in-situ administration of photosynthetic system rapidly conferred potent cardio-protection. Moreover, immunofluorescence staining was also analyzed. The MI group exhibited bright red fluorescence of HIF-1 $\alpha$  (Fig. 6K). Notably, both the BB group and the HCU (NIR) group exhibited a significant decrease of bright red fluorescence (Fig. 6G), indicating the alleviation of hypoxia in the myocardium induced by oxygen supply.

### Cardiac transcriptomic analysis of the HCU effect on MI

To decipher the mechanism of HCU-induced energy metabolic regulation and cardiac function recovery, we assessed transcriptomic profiling changes in mouse hearts. Heart tissues from KM mice (6-week) were subjected to RNA-seq analyses (N: normal group; M: MI

group; T: intramyocardial injection of HCU group). RNA-seq analysis identified an increase in expression of 1331 genes and a reduction in expression of 134 genes in MI hearts, while an increase in expression of 139 genes and a reduction in expression of 1550 genes in HCU-treated hearts (Fig. 7A, B and Supplementary Fig. 28a, b). Gene Ontology analysis revealed the up-regulated genes that were enriched in the mitochondrial respiratory chain complex and ATP synthase complex (Fig. 7C, D).

We found that mt-Atp8 (ATP synthase) and mt-Co2 (cytochrome c oxidase) mRNA levels were significantly increased in HCU-treated hearts compared to MI hearts (Fig. 7D). Analyses of HCU-treated transcriptome dataset revealed an increase in the expression of energy metabolic genes mt-Nd5 and mt-Atp8 along with cardiac muscle contraction gene Trdn (Fig. 7D). This was further supported by the

increased ATP synthesis as well as the increased CCO activity, in HCU-treated mice. Furthermore, GSEA analysis of KEGG pathway enrichment between HCU-treated hearts and MI hearts revealed significant differences in the enrichment of formation of ATP, cardiac muscle contraction, ABC transporter and apoptosis (Fig. 7E and Supplementary Fig. 28c, d). Together, these findings suggest that HCU treatment causes an improvement in mitochondrial oxidative respiration and cardiac functional recovery. Finally, a decrease in inflammation-related genes such as *Igkc* and *Jchain* was also observed, indicating good biocompatibility of HCU, consistent with serum and HE/Masson results (Fig. 7D). These findings suggested that HCU-induced energy metabolic regulation and cardiac function recovery.

### In vivo biocompatibility of HCU

The biocompatibility is essential for applications in biomedical fields. Therefore, we evaluated the biocompatibility of HCU. Before proceeding to in vivo experiments, we confirmed the negligible cytotoxicity of HCU in vitro, supporting its biocompatibility for further applications (Supplementary Fig. 11 and Supplementary Fig. 15). We administered HCU via intramyocardial injection in MI mice. After intramyocardial administration, the intrinsic fluorescence properties ( $\lambda_{\text{ex}}$ : 420 nm;  $\lambda_{\text{em}}$ : 680 nm) of *C. pyre* embedded in the HCU system were leveraged for fluorescence imaging. Due to the limited tissue penetration depth of fluorescence imaging, we performed ex vivo imaging of harvested hearts at predetermined time points (0, 1, 3, 5, 7, and 14 days post-injection) to track the fluorescence of *C. pyre*. Fluorescence signals were detectable in the heart for up to 7 days post-injection (Supplementary Fig. 29), indicating sustained retention and stability of HCU, which is critical for prolonged oxygenation therapy.

Moreover, during the treatment period, the body weight of mice in all groups demonstrated minimal fluctuation (Supplementary Fig. 30). Moreover, biocompatibility of the HU and HCU (NIR) was demonstrated by assays of cytokines TNF- $\alpha$ , IL-6, and IL-1 $\beta$ . As revealed by the assays, no significant differences were found among all groups, indicating that there was no inflammation in the organisms (Supplementary Fig. 31). Additionally, H&E staining of major organs revealed normal morphological features in all groups (Supplementary Fig. 32), suggesting that the photosynthetic system (HCU (NIR)) exhibited superior biocompatibility and biosafety.

### Discussion

In this study, the natural photosynthetic system (HCU) was successfully developed and applied in MI therapy to effectively improve the cardiac function of MI mice. Under near-infrared light irradiation, HCU enabled in situ photocrosslinking (365 nm), controllable oxygen supply (475 nm) and restoration of energy metabolism (800 nm). Specifically, in situ photosynthetic oxygen generation of *C. pyre* alleviated the hypoxic microenvironment, thereby mitigating hypoxia-induced mitochondrial damage and preventing cardiomyocyte apoptosis. Moreover, photobiomodulation activated cytochrome c oxidase (CCO) activity, thereby promoting the electron transport of mitochondrial respiration chain and enhancing energy metabolism. In the MI models, this photosynthetic system significantly alleviated cardiac injury and restored cardiac function. Based on the combination of photobiomodulation and micro-algae oxygen generation, the photosynthetic system effectively regulated energy metabolism and alleviated the hypoxic microenvironment, providing conceptual validation as a strategy for MI clinical treatment. Meanwhile, we hope in the future study we can focus on sonoluminescence of ultrasound to enhance tissue penetration and achieve clinical applications in ischemic diseases.

### Methods

#### Ethical statement

All experiments were performed in accordance with relevant guidelines and ethical regulations that were approved. All in vivo

experiments were approved by the Animal Ethics Committee of Shandong Normal University (AEECSNU2024123).

### Materials

The reagents CeCl<sub>3</sub>·6H<sub>2</sub>O (99.9%), YbCl<sub>3</sub>·6H<sub>2</sub>O (99.9%), TmCl<sub>3</sub>·6H<sub>2</sub>O (99.9%), Zr(NO<sub>3</sub>)<sub>4</sub>·5H<sub>2</sub>O (99.9%), (NH<sub>4</sub>)<sub>2</sub>S<sub>2</sub>O<sub>8</sub> (98.5%) were purchased from Macklin (China). Hyaluronic Acid (HA, 90%) was purchased from Heowns (China). NaOH (90%) and NH<sub>4</sub>F (96%) were purchased from Aladdin. C<sub>16</sub>H<sub>16</sub>LiO<sub>3</sub>P (LAP) photoinitiator was purchased from Engineering For Life Technology, Ltd. Annexin V-FITC Apoptosis Detection Kit, Mitochondrial membrane potential assay kit with JC-1, Cell mitochondria isolation kit, ATP Assay Kit, and DAPI were purchased from Beyotime Biotechnology. Micro Mitochondrial Respiratory Chain Complex IV Activity Assay Kit was purchased from Beijing Solarbio Science & Technology Co., Ltd. Annexin V-FITC/PI Apoptosis Detection Kit was purchased from Elabscience (Wuhan, China). The antibodies used are listed below: HIF-1 $\alpha$  (1:1000, BOSTER, China, Cat No. ZP1229BP29, Lot No. PB9253); Cyt c (1:5000, Zenbio, China, Cat No. R22867, Lot No. N19AP7P); C-Caspase3 (1:1000, Zenbio, China, Cat No. 341034, Lot No. N10AP01); Bcl-2 (1:1000, BOSTER, China, Cat No. BA0412, Lot No. 24 F 11 0305C19);  $\beta$ -Actin (1:1000, BOSTER, China, Cat No. BM0627, Lot No. 17K15B27). All reagents were used as purchased without further purification.

### Synthesis of NaCeF<sub>4</sub>:Yb,Tm,Zr UCNPs

NaCeF<sub>4</sub>:Yb,Tm,Zr UCNPs were synthesized using a modified hydrothermal method. Initially, 20 mmol of YbCl<sub>3</sub>·6H<sub>2</sub>O, 0.10 mmol of TmCl<sub>3</sub>·6H<sub>2</sub>O, 10 mmol of Zr(NO<sub>3</sub>)<sub>4</sub>·5H<sub>2</sub>O, and 69.9 mmol of CeCl<sub>3</sub>·6H<sub>2</sub>O were transferred to 5 mL deionized water. The mixture was stirred to form a uniform solution. Then, a specific quantity of NaOH and NH<sub>4</sub>F was added to the beaker. The obtained solution was further stirred for 30 min. After that, the mixture was transferred to the hydrothermal autoclave reactor. The temperature was increased by a gradient of 10 °C every 5 min and maintained at 200 °C for a period of 12 h. The solution after the hydrothermal reaction was centrifuged and washed for three times with anhydrous ethanol and deionized water. Finally, the above powders were dried in a vacuum drying oven at 60 °C. NaCeF<sub>4</sub>:Yb,Tm,Zr UCNPs doped with varying amounts of Zr were synthesized using the same method.

### Characterization of NaCeF<sub>4</sub>:Yb,Tm,Zr UCNPs

The appearance of UCNPs was analyzed using a Transmission Electron Microscope (HT7700, HITACHI, Japan). Additionally, dried UCNPs powders were examined by X-ray Diffraction Spectroscopy (XRD, Rigaku Smart Lab Se, Japan) at angles ranging from 5 to 90 degrees, and by X-ray Photoelectron Spectroscopy (XPS, ESCALAB250, Thermo Fisher, USA). The peaks of Ce, Yb, Tm, and Zr elements were analyzed semiquantitatively using Avantage software. The upconversion luminescence spectra of UCNPs were examined with a Fluorescence Spectrometer (FLS-1000, Edinburgh Instrument, UK) equipped with a 980 nm CW laser for excitation.

### In vitro degradation of NaCeF<sub>4</sub>:Yb/Tm/Zr

The as-synthesized NaCeF<sub>4</sub>:Yb/Tm/Zr UCNPs with a fixed amount of 30 mg in solid form were directly immersed in some buffers (3.0 mL) with different pH values, including monopotassium phosphate solution (pH 4.8), KH<sub>2</sub>PO<sub>4</sub>-K<sub>2</sub>HPO<sub>4</sub> buffer (pH 6.5), Hank's balanced salt solution (pH 7.4), sodium bicarbonate solution (pH 8.3), Tris-HCl (pH 8.8) and sodium hydroxide solution (pH 9.6). After being soaked for 48 h, the decrease in the integrated intensity of blue UCL signal for the as-synthesized NaCeF<sub>4</sub>:Yb/Tm/Zr UCNPs over time was monitored using a spectrometer equipped with a 980 nm diode laser (FLS1000, Edinburgh Instrument), and their corresponding UCL photographs were taken at different time points without using any filter. Meanwhile, the resulting supernatant was retrieved via filtration and then

subjected to elemental analyses using ICP-OES (Thermo Scientific iCAP 7400).

### Synthesis and characterization of HAMA

Hyaluronic acid (HA) was dissolved in distilled water at a concentration of 1% weight under magnetic stirring at 4 °C, and the pH was adjusted to 8 using 1 M NaOH. Subsequently, 5 equivalents of methacrylic acid (MA) were added in dark conditions, followed by the addition of a certain volume of 1 M NaOH to maintain the weak-base environment for 12 h. Finally, the sample was filtered using a PC membrane filter for 3 days and dried in a vacuum freeze dryer, and finally stored in a refrigerator under light-protected conditions. The chemical structures were studied by Fourier transform infrared spectroscopy to validate the success of HAMA (FT-IR, Nicolet 6700, Thermo Fisher, USA).

### C. pyre culture

*Chlorella pyrenoidosa* (*C. pyre*) was purchased from Nanjing Haiert Biotechnology Co. and cultured in 20 mL of BG11 medium (A137990, Thermo Fisher Scientific, MA, USA) in a conical flask with a vented cap. The cultures were maintained at 25 °C in an illumination incubator under a fixed diurnal cycle consisting of an 8-h light period followed by a 16-h dark period. A specified volume of fresh BG11 medium was added at 3-day intervals to compensate for evaporative losses. Once the cultures had developed a deep green color, half of the culture volume was replaced with fresh BG11 medium. The cyanobacteria were examined using an inverted fluorescence microscope (IX 71, Olympus, Japan) to confirm their purity.

### Photocrosslinking of HCU

*C. pyre* was harvested during the logarithmic growth stage, centrifuged at 4000 rpm for 5 min, and washed three times with PBS before the subsequent experiment. 50 mg/mL Hyaluronic acid methacrylate (HAMA),  $1 \times 10^8$  cells/mL *C. pyre*, and 30 µg/mL UCNPs (NaCeF<sub>4</sub>:Yb,Tm,Zr) were vigorously vortex-mixed. Other concentrations of HAMA/*C. pyre*/UCNPs biohybrid fluids could be simultaneously prepared by adjusting the concentrations of these components. Under 980 nm excitation at a power density of 1.0 W/cm<sup>2</sup>, the gel was crosslinked within 30 s by LAP. Scanning electron microscopy (SEM, GeminiSEM 500) was utilized to observe the morphology of UCNPs and lyophilized hydrogel.

### In situ photocrosslinking of HCU hydrogel

To assess the optical characterization of *C. pyrenoidosa* (*C. pyre*), upconversion nanoparticles (UCNPs), and lanthanum phosphate (LAP), aqueous dispersions of *C. pyre*, LAP, and UCNPs were prepared. UV-vis spectra were detected using a Cary5000 spectrophotometer (Agilent, USA) at wavelengths ranging from 200 to 900 nm. *Chlorella pyrenoidosa* was harvested during the logarithmic growth phase. It was then centrifuged at a rotational speed of 4000 rpm for 5 min and washed three times with phosphate-buffered saline (PBS) in preparation for subsequent experiments. *C. pyre*, hyaluronic acid methacrylate (HAMA), and UCNPs (NaCeF<sub>4</sub>:Yb,Tm,Zr) were vigorously vortex-mixed to final concentrations of 50 mg/mL,  $1 \times 10^8$  cells/mL, and 30 µg/mL, respectively. Other concentrations of HAMA/*C. pyre*/UCNPs biohybrid fluids can be simultaneously prepared by adjusting the concentrations of these components. The chicken tissue was cut with a thickness of 10 mm. 980 nm NIR laser (with 2 W·cm<sup>-2</sup>) was used to penetrate through chicken tissues and in situ cure the HCU inks.

### Measurement of photosynthetic oxygenation of HCU

Photosynthesis gel precursor (1 mL; containing 10 mg/mL HAMA,  $1 \times 10^8$  *C. pyre*, and 30 µg/mL UCNPs) was prepared and transferred to a 10 mL centrifuge tube with 5 mL PBS containing 10 mg of RDPP probe. A 660 nm laser was utilized for photosynthetic oxygenation. The

change in dissolved oxygen concentration was detected by the RDPP probe and recorded using a fluorometer.

### Adhesion properties assay of photosynthesis hydrogel

The adhesive properties of hydrogels were investigated using a macroscopic adhesion test. During the preparation of the adhesion test samples, HCU was poured into a cylindrical mold with dimensions of φ10 mm × 10 mm and subsequently crosslinked under the irradiation of 980 nm near-infrared (NIR) light. Different substrates were utilized to explore the adhesive characteristics of the hydrogels.

### Cell culture

Mouse cardiomyocytes (H9c2) and human umbilical vein endothelial cells (HUVECs) were obtained from Procell Life Science & Technology (Wuhan, China). H9c2 cells and HUVECs were cultured in DMEM supplemented with 10% fetal bovine serum (FBS) and 1% penicillin-streptomycin (P-S) at 37 °C in a humidified atmosphere containing 5% CO<sub>2</sub>.

### Primary cardiomyocyte isolation and culture

Primary cardiomyocytes (PCMs) from neonatal mice (2 days old) were isolated as described below. Briefly, the calcium and magnesium-free HBSS buffer, supplemented with 1% penicillin-streptomycin (P-S), was prepared. Heart tissues were isolated from 15 neonatal mice and washed with prepared HBSS buffer twice. Then these heart tissues were finely chopped and digested in an enzyme solution (type II collagen 0.0540 g in 30 mL calcium and magnesium-free HBSS buffer) on a magnetic stirrer (37 °C, 150 rpm) for 1.5 h. The CM growth medium, containing of 435 mL DMEM, 5 mL antibiotic-antimycotic (100×), 25 mL FBS, and 40 mL horse serum, was prepared. The supernatant was collected into a 50 mL centrifuge tube and then the CM growth medium was added at a volume ratio of 1:1. The mixture was then subjected to centrifugation at 700 rpm. The resultant clear layer was discarded, and the precipitate at the bottom of the tube was identified as CMs. These CMs were transferred to culture plates with CM growth medium for differential wall attachment. Finally, the floating PCMs (unattached) were collected after 1.5 h and seeded to various samples.

### In vitro biocompatibility assay

For CCK8 assay, H9c2 cells were seeded in 24-well cell culture plates ( $5 \times 10^4$  cells per well) and cultured under normoxia condition (21% O<sub>2</sub>) for 24 h. Subsequently, 24-well transwell chambers containing 0.25 mL HCU (containing  $1 \times 10^8$  cells/mL *C. pyre*) biohybrid fluids with different UCNPs concentrations were placed on top of these plates. The concentrations of HAMA and *C. pyre* were 10 mg/mL and  $1 \times 10^8$  cells/mL, respectively. The UCNPs concentrations in HCU varied as follows: 0, 0.2, 0.4, 0.6, 0.8, and 1.0 mg/mL. After another 24-hour incubation an CCK8 assay was conducted to evaluate cell viability.

For Live/Dead staining assay, human umbilical vein endothelial cells (HUVECs) were seeded on the glass-bottomed Petri dish, while 0.25 mL HCU (containing  $1 \times 10^8$  cells/mL *C. pyre*) were added in the culture medium. Cells were identified by Live/Dead staining assay after culturing for 5 days. For the Live/Dead staining assay, the cells were incubated with calcein-AM/propidium iodide (Beyotime, China) for 30 min at 37 °C. Finally, the fluorescence of *C. pyre* and calcein-AM/propidium iodide was examined using a Confocal Laser Scanning Microscope (Leica; STELLARIS 5).

### Establishment of hypoxia cells model

H9c2 cells were seeded in growth media at a density of  $5 \times 10^5$  cells per dish and cultured under normoxic conditions (21% O<sub>2</sub>) for 24 h. The medium in each dish, except for the normal group, was exchanged with glucose-free DMEM medium (1% penicillin-streptomycin). The cells in glucose-free DMEM medium were cultured in a 37 °C constant humidity incubator containing 94% N<sub>2</sub>, 5% CO<sub>2</sub> and 1% O<sub>2</sub> for 4 h

(simulating the process of cardiomyocyte ischemia), during which their status was monitored to confirm the successful establishment of the hypoxia model.

### HIF-1 $\alpha$ immunofluorescence assessment

Following a 4-hour incubation period under either normoxic (21% O<sub>2</sub>) or hypoxic (1% O<sub>2</sub>) conditions, with or without light irradiation, nine groups were established as follows: Normal group, MI group, NIR group (980 nm, 1.0 W/cm<sup>2</sup>, 20 min), HC group, HC (NIR) group, HU group, HU (NIR) group, HCU group, and HCU (NIR) group. Subsequently, each cell culture plate containing 1 mL PBS, HAMA/C. *pyre*, HAMA/UCNPs, or HAMA/C. *pyre*/UCNPs was placed on top of the cell culture plates. H9c2 and PCMs were fixed with 4% paraformaldehyde for 10 min, followed by permeabilization with 0.2% Triton X-100 in phosphate-buffered saline (PBS) for 8 min. HIF-1 $\alpha$  antibody were incubated overnight at 4 °C and secondary antibody was added for 1 h at room temperature in the dark. Nuclei were labeled with DAPI (G1012; Servicebio), and cells were visualized using a Leica 710 laser confocal microscope.

### In vitro cellular hypoxia alleviation

After construction of the hypoxia model, nine groups were established as follows: Normal group, Hypoxia group, NIR (980 nm, 1.0 W/cm<sup>2</sup>, 20 min) group, HC (HAMA/C. *pyre*) group, HC (NIR) group, HU (HAMA/UCNPs) group, HC (NIR) group, HCU (HAMA/C. *pyre*/UCNPs) group, HCU (NIR) group. The concentrations of HAMA, UCNPs, and C. *pyre* in all biohybrid fluids were 10 mg/mL, 30  $\mu$ g/mL and 1 $\times$ 10<sup>8</sup> cells/mL, respectively. Subsequently, each cell culture plate containing 1 mL PBS, HC, HU, or HCU were placed in a Stage Top Digital Gas Chamber, connected to a Leica TCS SP8 confocal laser scanning microscope. The chamber was set to maintain a hypoxic environment by controlling the gas mixture to consist of 1% O<sub>2</sub>, 5% CO<sub>2</sub>, and 94% N<sub>2</sub>. Then, [Ru(dpp)<sub>3</sub>] Cl<sub>2</sub> (Luminescent oxygen sensor) was utilized to detect the oxygen generation, and the observations were performed using confocal laser scanning microscopy (CLSM). Under a fluorescence microscope, cells were excited at 455 nm, and images of the red emission ( $\lambda$ <sub>max</sub>: 613 nm) were captured.

### Assessment of the activity of CCO

The activity of cytochrome c oxidase (CCO) was measured using a colorimetric assay with the Mitochondrial Respiration Chain Complex IV Activity Assay Kit (Solarbio Life Sciences, Beijing, China). Cells were initially inoculated into 96-well black plates. The experimental groups were then pre-treated under various conditions. All assays were conducted strictly in accordance with the manufacturer's guidelines. The CCO activity was quantified at a wavelength of 550 nm with an enzyme-labeled instrument (BioTek Synergy 2).

### Assessment of ATP level and ADP level

An ATP assay kit was used to evaluate the enhancement of intracellular ATP levels. H9c2 cells were seeded in culture dishes and allowed to reach 80% confluence. Initially, these cells were exposed to a hypoxic environment for 4 h. Subsequently, hydrogels were introduced and co-incubated with cells for 2 h before being subjected to 980 nm radiation for 20 min. The treated cells were then washed twice with PBS and lysed. After centrifugation at 12,000 g for 5 min at 4 °C, the supernatant of the cell lysate was obtained and assessed using an ATP assay working solution to evaluate the ATP level. After assessing the ATP level, 20  $\mu$ L of nucleotide-monitoring reagent was added to the solution, and the ATP levels were measured using an enzyme-labeled instrument (BioTek Synergy 2). After 10 min, the ADP in the solution was converted to ATP by adding 20  $\mu$ L of ADP converting reagent.

### Assessment of mitochondrial membrane potential assay (JC-1)

To investigate the protective effect of hydrogels on mitochondrial membrane potential under hypoxic conditions, a JC-1 assay kit was

utilized. Initially, H9c2 cells were seeded in glass-bottom cell culture dishes and cultured until they reached approximately 80% confluence. Subsequently, these cells were transferred to a hypoxic environment and incubated for 4 h. Thereafter, hydrogels were introduced, and the cells were co-incubated for 2 h. Subsequently, the cells were exposed to 980 nm radiation for 20 min. During this treatment, the cells always in a hypoxic environment. Following this, the treated-cells were washed twice with PBS and then incubated with the JC-1 staining working solution at 37 °C for 20 min. Subsequently, the cells were washed twice more with JC-1 staining buffer and then incubated in fresh culture medium. Finally, the mitochondrial membrane potential of H9c2 cells was visualized and recorded using confocal laser scanning microscopy. Additionally, the percentage of the JC-1 green fluorescent area in the cells was quantified using ImageJ software.

### Evaluation of apoptosis by flow cytometry

H9c2 cells were seeded in petri dishes at a density of 1  $\times$  10<sup>6</sup> cells. After an overnight incubation, the cells were treated with hypoxia for 4 h. Subsequently, hydrogels were added, and the cells were co-incubated for 2 h before being exposed to 980 nm radiation for 20 min. The Annexin V-FITC/PI Apoptosis Detection Kit was used to stain the cells for 15 min. Firstly, debris was excluded and target cell populations were identified using an FSC-A/SSC-A scatter plot. Following the removal of doublets through bimodal exclusion (FSC-H/FSC-A and SSC-W/SSC-H), live cells were distinguished using reactive dyes. Negative and positive populations were strictly defined based on comparisons between isotype controls and fluorescence minus one (FMO) controls. The threshold for positivity was set to encompass the fluorescence intensity of 99% of the control cells. This gating strategy ensured accurate clustering and consistent placement of gates across all experimental groups. Following this, cell samples were collected from the petri dishes by centrifugation, and the apoptotic cells were analyzed using flow cytometry.

### Western blot

After constructing the hypoxia model, four groups were established as follows: Normal group, Hypoxia group, HCU (HAMA/C. *pyre*/UCNPs) group, and HCU (NIR) group. The NIR group refers to "980 nm, 1.0 W/cm<sup>2</sup>, 20-min" exposure. Total proteins were extracted using RIPA lysis buffer supplemented with protease inhibitors, separated by SDS-PAGE, and transferred to a PVDF membrane (Millipore, Billerica, MA). The membrane was blocked with 5% non-fat milk at room temperature for 1 h and then incubated with the appropriate antibody. Protein bands were visualized using the chemiluminescent HRP detection system (Millipore, Billerica, MA). The antibodies used are listed below: HIF-1 $\alpha$  (1:1000, BOSTER, China, Cat No. ZP1229BP29, Lot No. PB9253); Cyt c (1:5000, Zenbio, China, Cat No. R22867, Lot No. N19AP7P); C-Caspase3 (1:1000, Zenbio, China, Cat No. 341034, Lot No. N10AP01); Bcl-2 (1:1000, BOSTER, China, Cat No. BA0412, Lot No. 24 F 11 0305C19);  $\beta$ -Actin (1:1000, BOSTER, China, Cat No. BM0627, Lot No. 17K15B27).

### Establishment of myocardial ischemic animal model

Adult KM mice (aged 6–8 weeks, male) were used to establish a myocardial ischemic animal model using isoproterenol (ISO, a non-selective  $\beta$ -adrenergic receptor agonist). Throughout the experiment, the animals had unrestricted access to food and water. They were randomly assigned to one of four groups: the Normal group, the MI group, the BB group (with a dosage of 20 mg/kg), and the HCU (NIR) group. Except for the Normal group, all other groups received intraperitoneal injections of ISO (8 mg/kg) for five consecutive days, while the Normal group was given an equivalent volume of PBS in the same manner. The mice were anesthetized using isoflurane (at a dosage of 0.1 mL/10 g) and placed in a supine position. Subsequently, a small amount of conductive adhesive was applied to the copper sheet of the physiological information

monitoring station, and the animals' paws were fixed to it, allowing for the acquisition of physiological information, including electrocardiogram (ECG) and respiration. The imaging target area was prepared by removing hair with a depilatory cream, and two-lead electrocardiogram electrodes were inserted to record the ECGs for a duration of 20 min. Immediately after the injection, echocardiography and Color Doppler Flow Imaging (CDFI) were performed using the Fujifilm Visual Sonics Vevo F2 system to confirm the success of the model induction.

### HCU treatment on MI mice

All animal experiments were performed under the ethics committee guidelines, and laboratory animals approved by Shandong Normal University Animal Ethics Committee. All the mice were assigned into 4 groups ( $n = 18$  per group). The mice in group 1 were untreated (Normal group), while mice in group 2–4 were MI mice. MI mice were prepared as described in supporting information. MI mice in group 2 were intramyocardially injected with PBS alone (MI group). MI mice in group 3 were oral ingested with Metoprolol Tartrate;  $\beta$ 1-adrenergic receptor antagonists alone (once every three days, BB group). MI mice in group 4 received an intramyocardial injection of HCU precursor under ultrasound guidance (50 mg/mL HAMA,  $1 \times 10^8$  cells/mL *C. pyre*, 30  $\mu$ g/mL UCNPs) at the ischemic border zone (once every three days, HCU (NIR) group). A 980 nm laser (1.0 W/cm<sup>2</sup>, 20 min/day for 7 days) was applied transcutaneously in HCU (NIR) group to crosslink the hydrogel and activate photosynthesis/CCO. Cardiac function was monitored by Echocardiography and Color Doppler Flow Imaging (Fujifilm Visual Sonics Vevo F2) pre-treatment and post-treatment (days 1, 3, 7, 30).

### Echocardiography test

One week following the establishment of the MI model, and 7 days post-HCU (NIR) therapy, the left ventricular (LV) functions of the mice were assessed using the IE33 echocardiography system (Vevo2100, Visual Sonics). M-mode and B-mode images, which reflect LV anterior wall morphology and beating activity, were recorded using the M250 transducer. The related indexes for evaluating cardiac function, such as fractional shortening (FS) and ejection fraction (EF), were calculated based on three consecutive cardiac cycles.

### Histological analysis

Seven days post-treatment, animals in 4 groups ( $n = 12$  per group) were euthanized. Hearts were harvested and sliced into 6  $\mu$ m thick paraffin sections. Histologic features of myocardial infarction (MI) were obtained using TTC (2,3,5-Triphenyltetrazolium Chloride), HE (Hematoxylin-eosin) staining, and Masson's Trichrome staining, following the manufacturers' instructions. The infarcted area of the heart was calculated based on the ratio of collagenous area (blue) to myocardial area (red). Data were analyzed using Image J and GraphPad Prism software.

### Immunofluorescence staining

The cardiac slices underwent a process of deparaffinization and rehydration. Subsequently, the tissue sections were immersed in EDTA antigen retrieval buffer and subjected to high-pressure steam treatment for 3 min to facilitate antigen retrieval. After natural cooling, the sections were transferred to PBS (pH 7.4) and gently agitated on a decolorization shaker. Then, the sections were incubated with a 10% goat serum solution at 37 °C for 2 h. An appropriate amount of primary antibody, proportioned as per the experimental requirements, was added to the sections and incubated overnight at 4 °C in a humid chamber. Following several washes in PBS, the secondary antibody was applied to cover the tissue and incubated for 2 h at 37 °C. Finally, a DAPI-containing blocker was added dropwise and incubated at room temperature for 10 min.

### RNA-seq analysis

Heart tissue from each treatment group in MI mice (Normal group,  $n = 3$ ; MI group,  $n = 3$ ; intramyocardial injection of HCU group,  $n = 3$ ) was collected, and total RNA was extracted. The purity of the RNA was assessed using a NanoDrop 2000/c spectrophotometer (Thermo Scientific). Subsequently, libraries were constructed utilizing the VAHTS Universal V6 RNA-seq Library Prep Kit. The transcriptome sequencing and subsequent analysis were performed by SHBIO Biotech. Agilent 4200 bioanalyzer was employed to evaluate the concentration and size distribution of cDNA library. The libraries were sequenced using the Illumina NovaSeq 6000 platform, generating paired-end reads of 150 bp. The high-throughput sequencing protocol was strictly adhered to in accordance with the manufacturer's instructions (Illumina). The raw reads were filtered using Seqtk prior to mapping to the genome with Hisat2 (version 2.0.4) [1, Supporting Information]. Gene fragments were quantified employing StringTie (v1.3.3b), followed by normalization using TMM (trimmed mean of M values) [2–5, Supporting Information]. Significantly differentially expressed genes (DEGs) were identified based on a False Discovery Rate (FDR) threshold of  $Q < 0.05$  and a fold change greater than 2, utilizing edgeR software for the analysis [5–8, Supporting Information]. The hypergeometric distribution of the differentially expressed genes (DEGs) was validated. R version 3.2.0 was utilized to conduct Gene Ontology (GO) and Kyoto Encyclopedia of Genes and Genomes (KEGG) pathway enrichment analyses, as well as to generate the corresponding figures. Bioinformatic analyses were conducted using an online platform available at <https://www.bioinformatics.com.cn>.

### Long-term in situ retention of HCU

6-week-old male KM mice bearing MI ( $n = 3$ ) were administered intramyocardial injection of HCU. Hearts were removed at 0, 1, 3, 5, 7, 14, and 30 days after injection and observed using an in vivo imaging system (PerkinElmer, USA) with excitation at 420 nm. The bioluminescence of *C. pyre* was measured, which was further quantified using the software Image J.

### Biological safety

To assess the potential toxicity and inflammation resulting from the HCU, blood samples were collected after a 7-day treatment period. Enzyme-linked immunosorbent assays (ELISAs) were conducted using serum to test the levels of TNF- $\alpha$ , IL-6, and IL-1 $\beta$ . The major organs (liver, spleen, lung, kidney) of mice were collected for in vivo toxicity analysis. Hematoxylin and eosin (H&E) and Masson's trichrome staining were used to evaluate the damage to the mice's major organs. Simultaneously, images were observed and collected using the Digital Slice Scanner (3D HISTECH).

### Statistical analysis

All experiments were conducted independently and repeated to ensure the reliability of the data presented in the figures. Data are depicted as error bars representing the mean or geometric mean  $\pm$  standard deviation (S.D.). Statistical significance was determined using unpaired two-tailed Student's *t* test. Significance levels are indicated by the exact *P* value presented in the figures. To mitigate potential bias, no data were excluded, samples were randomly assigned to experimental groups, organisms were cultured under consistent environmental conditions, and randomization was employed in group assignments. Investigators were not blinded during data collection and analysis.

### Reporting summary

Further information on research design is available in the Nature Portfolio Reporting Summary linked to this article.

## Data availability

All data generated in this study are provided in the Supplementary Information/Source Data file. RNA-seq data are deposited in SRA under accession code [PRJNA1301596](https://www.ncbi.nlm.nih.gov/sra/PRJNA1301596). Source data are provided with this paper.

## References

- Melo, P. et al. Effects of intracoronary supersaturated oxygen infusion on the time course of myocardial blood flow and extent of microvascular obstruction in an ischemia/reperfusion preclinical swine model. *Eur. Heart J.* **10**, 45 (2024).
- Shi H. et al. Global burden of ischemic heart disease from 2022 to 2050: projections of incidence, prevalence, deaths, and disability-adjusted life years. *Eur. Heart J.-Qual. Care Clin. Outcomes.* **11**, 355–366, (2024).
- Ritterhoff, J. & Tian, R. Metabolic mechanisms in physiological and pathological cardiac hypertrophy: new paradigms and challenges. *Nat. Rev. Cardiol.* **20**, 812–829 (2023).
- Zhao, Z., Ukidve, A., Kim, J. & Mitragotri, S. Targeting strategies for tissue-specific drug delivery. *Cell* **181**, 151–167 (2020).
- Harmouch, K. M. et al. The efficacy of different revascularization strategies in patients with acute myocardial infarction and multi-vessel coronary artery disease: an updated meta-analysis. *J. Am. Coll. Cardiol.* **83**, 1011 (2024).
- Virani, S. S. et al. 2023 AHA/ACC/ACCP/ASPC/ NLA/PCNA guideline for the management of patients with chronic coronary disease: a report of the American Heart Association/American College of Cardiology Joint Committee on clinical practice guidelines. *J. Am. Coll. Cardiol.* **82**, 833–955 (2023).
- Maghfour, J. et al. Photobiomodulation CME part I: Overview and mechanism of action. *J. Am. Acad. Dermatol.* **91**, 793–802 (2024).
- Wang, Z. X. & Kim, S. H. Effect of photobiomodulation therapy (660 nm) on wound healing of rat skin infected by *Staphylococcus*. *Photobiomodul Photomed. Laser Surg.* **38**, 419–424 (2020).
- Ferroni, L. et al. Fluorescent light energy (FLE) acts on mitochondrial physiology improving wound healing. *J. Clin. Med.* **9**, 559 (2020).
- Wan, Z. et al. NIR light-assisted phototherapies for bone-related diseases and bone tissue regeneration: a systematic review. *Theranostics* **10**, 11837–11861 (2020).
- Salehpour, F. et al. Transcranial low-level laser therapy improves brain mitochondrial function and cognitive impairment in D-galactose-induced aging mice. *Neurobiol. Aging* **58**, 140–150 (2017).
- Reinhart, F. et al. 810 nm Near-Infrared Light Offers Neuroprotection and Improves Locomotor Activity in MPTP-Treated Mice. *Neurosci. Res.* **92**, 86–90 (2015).
- Zorzo, C., Rodríguez-Fernández, L., Martínez, J. A. & Arias, J. L. Photobiomodulation increases brain metabolic activity through a combination of 810 and 660 wavelengths: a comparative study in male and female rats. *Lasers Med Sci.* **39**, 1 (2024).
- Pinke, G., Zhou, L. & Sazanov, L. A. Cryo-EM structure of the entire mammalian F-type ATP synthase. *Nat. Struct. Mol. Biol.* **27**, 1077–1085 (2020).
- Kadenbach, B. Complex IV—the regulatory center of mitochondrial oxidative phosphorylation. *Mitochondrion* **58**, 296–302 (2021).
- Zhao, C. et al. Transcranial photobiomodulation enhances visual working memory capacity in humans. *Sci. Adv.* **8**, eabq3211 (2022).
- Vercellino, I. & Sazanov, L. A. The assembly, regulation and function of the mitochondrial respiratory chain. *Nat. Rev. Mol. Cell Biol.* **23**, 141–161 (2022).
- Zhao, Y. et al. Hypoxia-induced signaling in the cardiovascular system: pathogenesis and therapeutic targets. *Signal Transduct. Target. Ther.* **8**, 431 (2023).
- Chen, P. et al. A plant-derived natural photosynthetic system for improving cell anabolism. *Nature* **612**, 546–554 (2022).
- Seymour, J. et al. Zooming in on the phycosphere: the ecological interface for phytoplankton–bacteria relationships. *Nat. Microbiol.* **2**, 17065 (2017).
- Xiong, W. et al. Microalgae-material hybrid for enhanced photosynthetic energy conversion: a promising path towards carbon neutrality. *Natl. Sci. Rev.* **10**, nwad 200 (2023).
- Burlacot, A. et al. Alternative photosynthesis pathways drive the algal CO<sub>2</sub> concentrating mechanism. *Nature* **605**, 366–371 (2022).
- Wang, J. et al. Oxygen-generating cyanobacteria powered by upconversion nanoparticles-converted near-infrared light for ischemic stroke treatment. *Nano Lett.* **21**, 4654–4665 (2021).
- Zhang, F. et al. Biohybrid microrobots locally and actively deliver drug-loaded nanoparticles to inhibit the progression of lung metastasis. *Sci. Adv.* **10**, eadn6157 (2024).
- Qiao, Y. et al. Engineered algae: A novel oxygen-generating system for effective treatment of hypoxic cancer. *Sci. Adv.* **6**, 5996 (2020).
- Kang, Y. et al. Programmed microalgae-gel promotes chronic wound healing in diabetes. *Nat. Commun.* **15**, 1042 (2024).
- Zhong, D. et al. Orally deliverable strategy based on microalgal biomass for intestinal disease treatment. *Sci. Adv.* **7**, 9265 (2021).
- Tarsitano, M. et al. Chlorella-enriched hydrogels protect against myocardial damage and reactive oxygen species production in an in vitro ischemia/reperfusion model using cardiac spheroids. *Biofabrication* **17**, 015006 (2025).
- Zhang, C. et al. In situ formed microalgae-integrated living hydrogel for enhanced tumor starvation therapy and immunotherapy through photosynthetic oxygenation. *Nano Lett.* **24**, 3801–3810 (2024).
- Yang, Y. et al. Metal doping enabling defective CoMo-layered double hydroxide nanosheets as highly efficient photosensitizers for NIR-II photodynamic cancer therapy. *Adv. Mater.* **37**, 2405847 (2024).
- Teh, D. B. L. et al. A flexi-PEGDA upconversion implant for wireless brain photodynamic therapy. *Adv. Mater.* **32**, 2001459 (2020).
- Chen, C. et al. Multi-photon near-infrared emission saturation nanoscopy using upconversion nanoparticles. *Nat. Commun.* **9**, 3290 (2018).
- Ding, B. et al. Biodegradable upconversion nanoparticles induce pyroptosis for cancer immunotherapy. *Nano Lett.* **21**, 8281–8289 (2021).

## Acknowledgements

This work was supported by the National Natural Science Foundation of China (22134004 to B.T., 22376128 to W.G., 22576122 to W.G., 22404099 to Y.T.), the Natural Science Foundation of Shandong Province of China (ZR2024MB046 to Y.T., 2024HWYQ-014 to Y.T.), Taishan Scholars Program of Shandong Province (tsqn.202312336 to Y.T.), the Major Science and Technology Innovation Project of Shandong Province (2021ZDSYS09 to W.G.), and the Analysis and Test Center of College of Chemistry, Chemical Engineering and Materials Science, Shandong Normal University.

## Author contributions

These authors contributed equally: Y.C. and L.L. Y.C., W.G. and B.T. designed research; L.L. and Y.C. performed research, assisted by Z.C., X.H. and Y.W.; Y.C. and L.L. wrote the paper, assisted by W.G. and Y.T. All authors have given approval to the final version of the manuscript.

## Competing interests

The authors declare no competing interests.

## Additional information

**Supplementary information** The online version contains supplementary material available at <https://doi.org/10.1038/s41467-025-63749-9>.

**Correspondence** and requests for materials should be addressed to Yue Tang, Wen Gao or Bo Tang.

**Peer review information** *Nature Communications* thanks Carmine Gentile, and Xiaolei Wang for their contribution to the peer review of this work. A peer review file is available.

**Reprints and permissions information** is available at <http://www.nature.com/reprints>

**Publisher's note** Springer Nature remains neutral with regard to jurisdictional claims in published maps and institutional affiliations.

**Open Access** This article is licensed under a Creative Commons Attribution-NonCommercial-NoDerivatives 4.0 International License, which permits any non-commercial use, sharing, distribution and reproduction in any medium or format, as long as you give appropriate credit to the original author(s) and the source, provide a link to the Creative Commons licence, and indicate if you modified the licensed material. You do not have permission under this licence to share adapted material derived from this article or parts of it. The images or other third party material in this article are included in the article's Creative Commons licence, unless indicated otherwise in a credit line to the material. If material is not included in the article's Creative Commons licence and your intended use is not permitted by statutory regulation or exceeds the permitted use, you will need to obtain permission directly from the copyright holder. To view a copy of this licence, visit <http://creativecommons.org/licenses/by-nc-nd/4.0/>.

© The Author(s) 2025